

Probing the topologically trivial nature of end states in antiferromagnetic atomic chains on superconductors

Received: 9 November 2022

Accepted: 25 April 2023

Published online: 12 May 2023

 Check for updatesLucas Schneider¹, Philip Beck¹, Levente Rózsa^{2,3,4}, Thore Posske^{5,6}, Jens Wiebe¹✉ & Roland Wiesendanger¹

Spin chains proximitized by *s*-wave superconductors are predicted to enter a mini-gapped phase with topologically protected Majorana modes (MMs) localized at their ends. However, the presence of non-topological end states mimicking MM properties can hinder their unambiguous observation. Here, we report on a direct method to exclude the non-local nature of end states via scanning tunneling spectroscopy by introducing a locally perturbing defect on one of the chain's ends. We apply this method to particular end states observed in antiferromagnetic spin chains within a large minigap, thereby proving their topologically trivial character. A minimal model shows that, while wide trivial minigaps hosting end states are easily achieved in antiferromagnetic spin chains, unrealistically large spin-orbit coupling is required to drive the system into a topologically gapped phase with MMs. The methodology of perturbing candidate topological edge modes in future experiments is a powerful tool to probe their stability against local disorder.

Hybrid systems of magnetic and superconducting materials in reduced dimensions have been of great interest in recent years, owing to the exciting emergent physics such as unconventional superconductivity and topological edge modes expected in these platforms^{1–6}. In particular, there has recently been a focus on antiferromagnetic materials proximity coupled to *s*-wave superconductors^{7–11}. Since antiferromagnets possess no net magnetic moment in their magnetic unit cell, they do not have considerable stray fields which would destroy superconducting order. A coexistence of antiferromagnetism and superconductivity in, e.g., thin films on *s*-wave superconductors⁸ or the Fe-based superconductors^{12,13} was previously explained by the large size of Cooper pairs compared to the magnetic unit cell of the materials or by an unconventional s_{\pm} type pairing symmetry¹⁴. The absence of the net magnetic moment also gives rise to an effective

time-reversal symmetry (ETRS) in an antiferromagnet, consisting of physical time reversal inverting the spin directions and a spatial symmetry exchanging the antiferromagnetic sublattices.

In the limit of a single magnetic adatom or molecule on a superconducting surface, the interaction of its spin with the host material induces local quasiparticle states inside the superconducting gap known as Yu-Shiba-Rusinov (YSR) states^{15–17}. When multiple of these impurities are close to each other, their YSR states split in energy as they start to couple^{18,19}. Without spin-orbit coupling (SOC), such a splitting would be prohibited by the ETRS for a strictly antiferromagnetic alignment of the spins in adatom pairs^{18,20}. However, it has been shown recently that the splitting is allowed in the presence of SOC on a surface^{19,21}. In larger arrays of magnetic impurities, the coupled YSR states form YSR sub-gap bands, which can potentially have

¹Department of Physics, University of Hamburg, D-20355 Hamburg, Germany. ²Department of Physics, University of Konstanz, D-78457 Konstanz, Germany.

³Department of Theoretical Solid State Physics, Institute of Solid State Physics and Optics, Wigner Research Centre for Physics, H-1525 Budapest, Hungary.

⁴Department of Theoretical Physics, Budapest University of Technology and Economics, H-1111 Budapest, Hungary. ⁵I. Institute for Theoretical Physics, University of Hamburg, D-22607 Hamburg, Germany. ⁶Centre for Ultrafast Imaging, Luruper Chaussee 149, D-22761 Hamburg, Germany.

✉ e-mail: jwiebe@physnet.uni-hamburg.de

non-trivial topology^{3–6,22,23} and lead to the emergence of topologically protected Majorana modes (MMs) at the edges of the array^{24–28}. In one dimension, a chain of magnetic impurities with topologically non-trivial YSR bands is expected to host zero-energy MMs at both ends for sufficient chain length. The Majorana number in spin chains can be interpreted as the parity of the number of spin-polarized bands crossing the Fermi level in the absence of superconducting pairing terms (c.f. Methods, Eq. (8)). Without SOC, the ETRS in antiferromagnetic chains leads to doubly degenerate excitations in the magnetic Brillouin zone. Thus, there is necessarily an even number of band crossings and a topologically trivial Majorana number. However, finite SOC breaks this symmetry and the degeneracies can be lifted. Thus, SOC or certain spatial symmetries theoretically open up possibilities for topologically non-trivial phases hosting MMs also in antiferromagnetic chains^{9,10}. Experimental investigations of the low-energy electronic structure with a focus on such modes so far largely concentrated on ferromagnetic chains^{25,27,29–35} and a few on spin-spirals^{24,36}, but studies of the antiferromagnetic case are sparse³⁴.

A general problem with the interpretation of such experimental data is the fact that near-zero-energy states can always appear as artifacts—e.g., induced by local defects or by a different electronic structure at the chain termination—in local tunneling spectroscopy measurements^{33,34,36}. Therefore, a good understanding of the sample's underlying YSR band structure and its direct correlation with the observation of end states is clearly desired to pin down the nature of these end states. In this work, we additionally pursue a new strategy to test the MM nature of end states residing in a comparably large bulk minigap which we observed for scanning-tunnel-microscope-(STM)-tip-constructed³⁷ antiferromagnetic Mn chains on the atomically clean surfaces of Nb(110) and Ta(110): We intentionally locally perturb one

end of the chain with a local defect. While MMs residing in a topological minigap which is wider in energy than the perturbation's energy scale are expected to remain either completely unaffected or will merely laterally shift, trivial end states will split in energy only on the perturbed side of the chain (see Supplementary Note 1). We compare the experimental findings to an effective single-particle model for an antiferromagnetic spin chain coupled to an *s*-wave superconductor.

Results

Antiferromagnetic Mn chains on Nb(110)

Single Mn atoms on clean Nb(110) and Ta(110) surfaces have been studied both experimentally^{19,27,29,32,38,39} and theoretically^{40–43}, and offer a suitable platform for studying well-defined YSR arrays. In particular, it has been shown that the magnetic interaction between neighboring adatoms can be tuned from ferromagnetic to antiferromagnetic when varying the inter-atomic distance and the crystallographic direction connecting the atoms on the surface^{19,38}. Spin-polarized measurements have revealed that densely packed linear chains of Mn atoms constructed along the $[1\bar{1}\bar{1}]$ direction of the (110) surfaces (Fig. 1a) of Nb³⁸ and Ta (Supplementary Fig. 2) feature an out-of-plane antiferromagnetic ground state, in agreement with ab-initio calculations⁴².

We start by presenting the results on antiferromagnetic Mn chains on Nb(110): Fig. 1b shows the topography of a Mn₄₀ chain together with examples of deconvoluted dI/dV maps obtained at sub-gap energies ($\Delta_{\text{Nb}} = 1.51$ meV, see Methods, Supplementary Note 3 and Supplementary Fig. 3). A dI/dV line profile along the same chain is presented in Fig. 1d. Additionally, the evolution of the sub-gap local density of states (LDOS) for Mn_{*N*} chains on Nb(110) with increasing number of sites *N* is shown in Fig. 1c, separately for the chain's left end (left panel), for the chain's bulk (central panel) and for the right end (right panel).

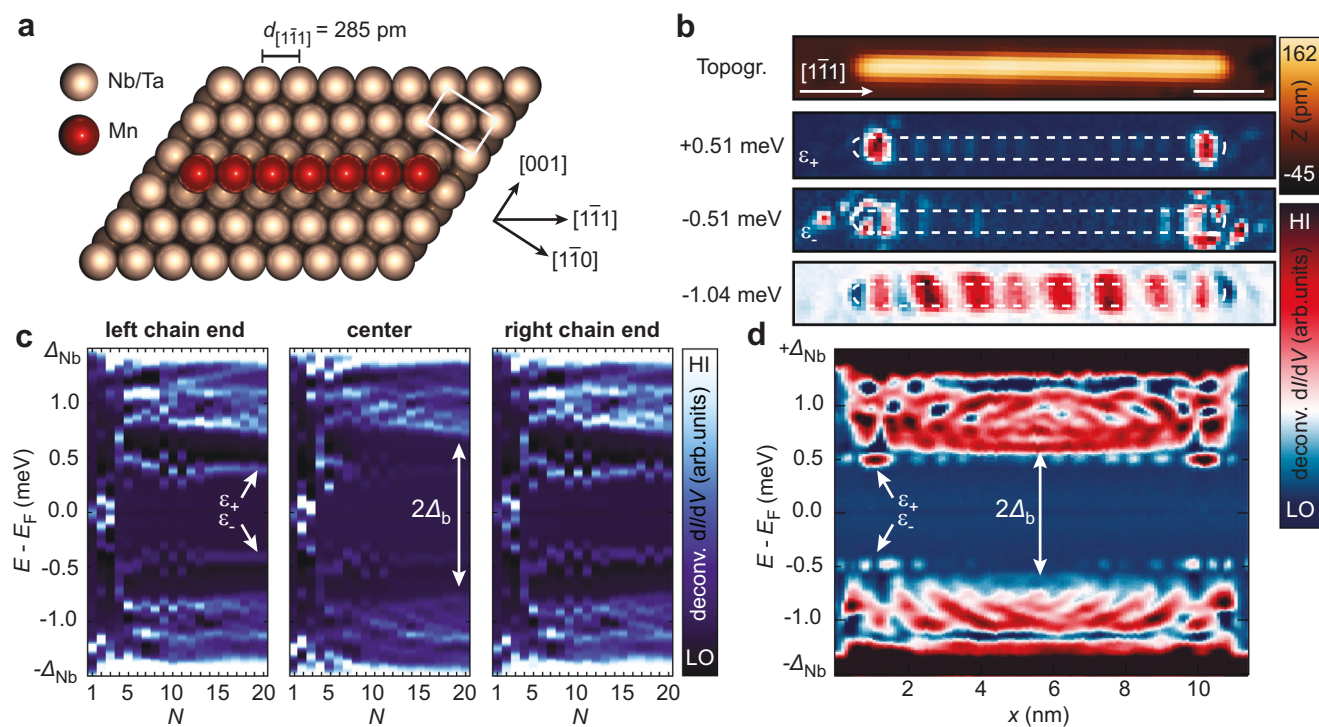


Fig. 1 | Geometry and low-energy electronic structure of antiferromagnetic Mn chains on Nb(110). **a** Sketch of Mn adatoms (red) positioned on neighboring hollow sites of the Nb(110) or Ta(110) lattice (beige) along the $[1\bar{1}\bar{1}]$ direction. **b** Constant-current STM image (topography, top panel) of a Mn₄₀ chain and simultaneously acquired deconvoluted dI/dV maps (bottom panels) at selected energies as indicated. The white scale bar corresponds to 2 nm. The apparent extent of the chain from the top panel is marked by white dashed boundaries. **c** Sequence of

deconvoluted dI/dV spectra measured on the left end, in the center and on the right end of Mn_{*N*} chains with increasing number of sites *N*. The emergence of the chain's bulk minigap Δ_b and of finite-energy end states $\epsilon_{+/-}$ are indicated. Note that single atoms are added only to the right chain end during this measurement. **d** Deconvoluted dI/dV line-profile measured along the longitudinal axis through the center of the Mn₄₀ chain. The lateral position of the spectra is aligned with the topography in panel b. Parameters: $V_{\text{stab}} = -6$ mV, $I_{\text{stab}} = 1$ nA, $V_{\text{mod}} = 20$ μ V.

There is a continuum of states visible in the energy range of $0.7 \text{ meV} < |E| < 1.5 \text{ meV}$, exhibiting standing-wave patterns (c.f. Fig. 1d and the map at -1.04 meV in Fig. 1b) due to quasiparticle interference (QPI). This indicates the formation of dispersive YSR bands^{27,32,34} which we analyze later on. In contrast to this, no bulk states are observed within a gapped region of $\pm\Delta_b = \pm 0.7 \text{ meV}$ for chain lengths exceeding $N = 6$ sites. This is a surprising result since the maximal gaps previously found in dispersive YSR bands in ferromagnetic spin chains on superconducting surfaces were on the order of $50\text{--}180 \mu\text{eV}$ ^{24,27,30,32,44}.

Inside the minigap Δ_b , we find clearly localized end states at energies $\varepsilon_{+/-} = \pm 0.51 \text{ meV}$ (Fig. 1b). In addition to the end-state nature of these features, a small oscillatory component of their wave function is found to decay into the chain's bulk (see Fig. 1b, d). As it can be seen in Fig. 1c, these energetically isolated states form at energies $\varepsilon_{+/-}$ already for $N > 5$ and their energy is only faintly oscillating in energy for longer systems. This fast convergence of the end-state energy with increasing chain length agrees with the good localization of the features, i.e., interactions between the ends already vanish for short chains. Notably, the end states in the regime $8 < N < 14$ are energetically split into four eigenstates for odd N while there are only two eigenstates for even N (see Fig. 1c).

Comparison to antiferromagnetic Mn chains on Ta(110)

In order to further investigate experimentally whether the appearance of such low-energy end states is a consequence of the antiferromagnetic spin alignment in the chain and thus not limited to only one experimental platform, we study structurally similar Mn chains on a clean Ta(110) surface ($\Delta_{\text{Ta}} = 0.64 \text{ meV}$). It has been shown previously that Mn atoms on a Ta(110) surface exhibit surprising similarities to Mn/Nb(110)^{29,39} due to the identical number of valence electrons and the same crystal structure of the substrates, however, with a strongly enhanced SOC in Ta compared to Nb. Most notably, densely packed Mn chains along the $[\bar{1}\bar{1}1]$ direction are also found to be antiferromagnetically ordered (see Supplementary Fig. 2). Measurements of the low-energy electronic structure in these chains are presented in Fig. 2. The dI/dV maps in Fig. 2a measured around a Mn_{22} chain reveal the presence of well-localized end states with near-zero energy and a similar spatial appearance as the end states found in Mn chains on Nb(110), while higher-energy excitations are mostly localized in the chain's bulk. Furthermore, a weak oscillatory pattern can be seen in the map obtained at -0.28 meV , indicating the presence of QPI in the bulk states of this platform as well. The dI/dV line-profile along a Mn_{20} chain shown in Fig. 2b suggests that the bulk of the chain is electronically gapped by a minigap $\pm\Delta_b = \pm 0.2 \text{ meV}$. Figure 2c shows the length dependence of the LDOS features for chains with $10 < N < 22$. Here, it is also visible that end states of almost constant energy are present on both chain ends while the bulk remains gapped. On the left, unperturbed end, a damped even-odd oscillation in the end-state energies is observed again, as for the Nb case. The overall appearance of the low-energy electronic structure is very similar to Mn/Nb(110). It is therefore natural to conjecture that the end states in the Mn/Ta(110) platform have a similar origin as in the Mn/Nb(110) case. However, since the end states in Mn/Ta(110) are very close to or at zero energy, the question arises whether or not this system realizes a topological superconductor with the accompanying near-zero energy MMs at its ends.

Perturbation of the end states by local defects

For testing the topologically non-trivial or trivial nature of the end states, the influence of local defects on the end states in Mn/Nb(110) and Mn/Ta(110) chains is studied. These defects can be either of magnetic or of non-magnetic origin. It has been shown previously that the energy of individual YSR states is very sensitive to

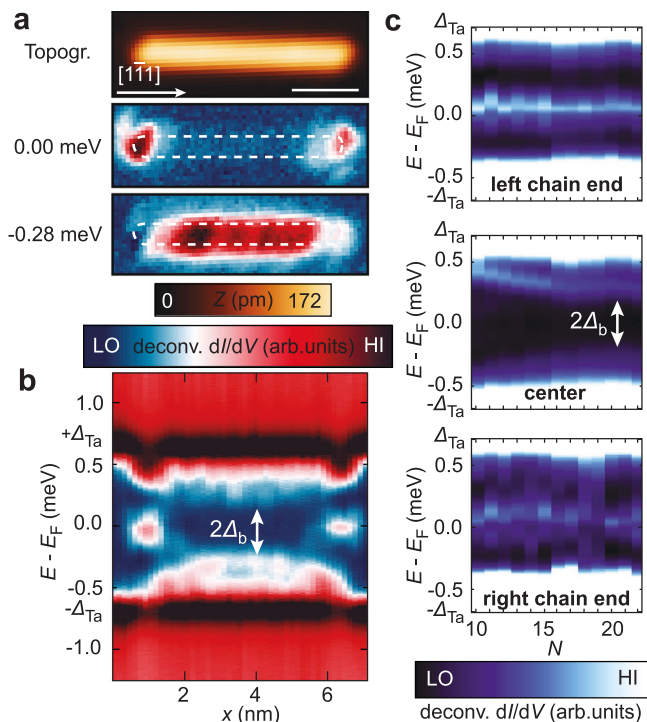


Fig. 2 | Sub-gap electronic structure of antiferromagnetic Mn chains on Ta(110).

a Constant-current STM image (topography, top panel) of a Mn_{22} chain and simultaneously acquired deconvoluted dI/dV maps (bottom panels) at selected energies as indicated. The white scale bar corresponds to 2 nm . The apparent extent of the chain from the top panel is marked by white dashed boundaries. **b** Deconvoluted dI/dV line-profile measured along the longitudinal axis through the center of a Mn_{20} chain. The lateral position of the spectra is aligned with the topography in **a**. The arrow indicates the chain's bulk minigap. **c** Sequence of deconvoluted dI/dV spectra measured at the left end, in the center and at the right end of Mn_N chains with increasing number of sites N . The emergence of a bulk minigap Δ_b (marked) and of end states with energies close to the Fermi energy E_F can be observed. Parameters: $V_{\text{stab}} = -2.5 \text{ mV}$, $I_{\text{stab}} = 1 \text{ nA}$, $V_{\text{mod}} = 20 \mu\text{V}$.

variations in adsorption geometries^{45,46}, defects like local oxygen impurities⁴⁷, or local charge density⁴⁸. Also hydrogenation of adatoms has been shown to drastically alter their magnetic properties and, importantly, their exchange coupling to the substrate⁴⁹. Since the exchange coupling strength is one of the main factors determining the YSR state energies of magnetic impurities¹⁷, hydrogenated Mn atoms at the end of the chain are expected to have clearly shifted YSR state energies compared to unperturbed Mn atoms. Figure 3a shows an example of a Mn_{20} chain on Nb(110) with a dark spot visible on the left side of the chain, which is presumably adsorbed hydrogen or another weakly bound surface adsorbate trapped at an oxygen defect of the Nb(110) surface. When measuring dI/dV maps at sub-gap energies on this Mn chain, the left and the right end state have slightly different energies ($\pm 0.43 \text{ meV}$ and $\pm 0.35 \text{ meV}$, respectively, see Supplementary Note 4 for details). When removing the defect next to the chain by local voltage pulses (Fig. 3b), both end states appear at the same energy ($\pm 0.35 \text{ meV}$) again. A similar effect can actually be seen in the data of Fig. 1c already where the end state on the right end is found to oscillate in energy for $15 < N < 20$ while the state on the left end remains at fixed energy. This unambiguously proves the local nature of these states, in clear contrast to non-local, spatially correlated states like MMs or their precursors²⁷ (see Supplementary Note 1 for the effect of potential disorder within a minimal model for antiferromagnetic YSR chains). Note at this point that although the finite energy of the

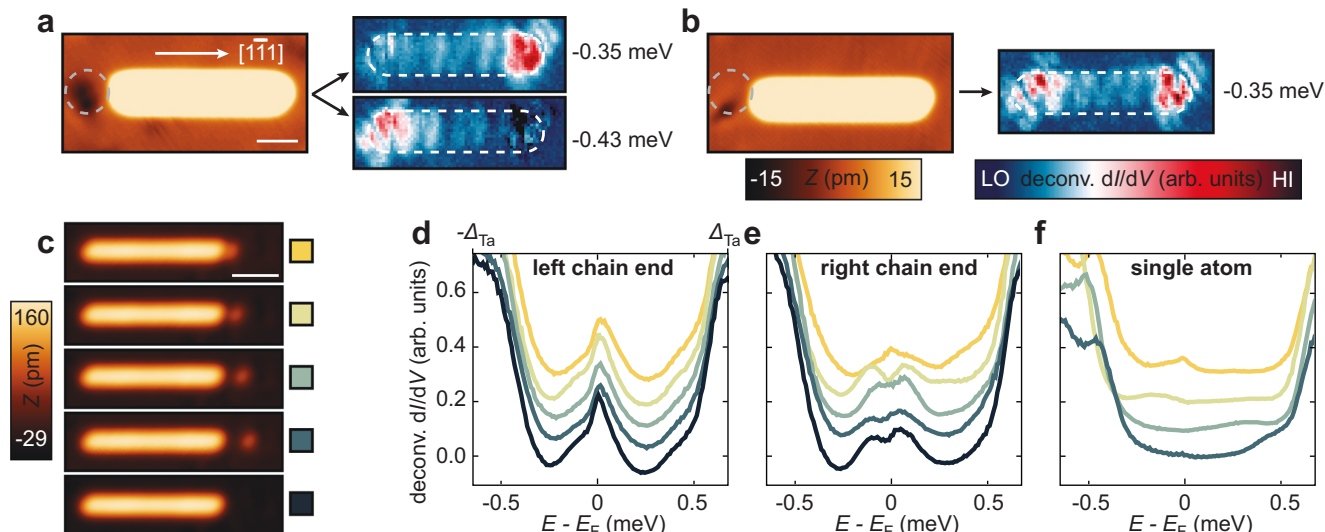


Fig. 3 | Response of the end state energies to local defects. **a** Constant-current image of a Mn_{20} chain on Nb(110) (left panel) with adjusted contrast to highlight the defect on the left side of the image which is marked by the gray dashed circle. The white scale bar corresponds to 1 nm. Deconvoluted dI/dV maps at selected energies (right panels) reveal that the two end states have different energies. The apparent extent of the chain from the left panel is marked by white dashed boundaries. **b** Constant-current image of the same Mn_{20} chain after applying bias voltage pulses to remove the local defect. A deconvoluted dI/dV map at a selected energy (right) shows that the end states now have equal energy. Parameters: $V_{\text{stab}} = -6$ mV,

$I_{\text{stab}} = 1$ nA, $V_{\text{mod}} = 20$ μV . **c** Constant-current STM images of a Mn_{22} chain on Ta(110) and a single Mn atom which is subsequently moved to positions with different distances from the right chain end. The bottommost panel shows the unperturbed chain. The white bar corresponds to 2 nm. Parameters: $V_{\text{stab}} = -20$ mV, $I_{\text{stab}} = 0.2$ nA. **d** Deconvoluted dI/dV spectra measured on the left chain end, **e**, on the right chain end and **f**, on the single Mn atom for the different adatom distances depicted in **c**. The spectra are vertically offset for clarity. Their color indicates which panel in **c** they belong to. Parameters: $V_{\text{stab}} = -2.5$ mV, $I_{\text{stab}} = 1$ nA, $V_{\text{mod}} = 20$ μV .

end states already suggested their topologically trivial origin, it has been shown previously that topological states may remain at finite energies even for long chains due to fine-tuned interactions⁵⁰.

We performed a similar experiment for Mn chains on Ta(110) using a single Mn atom as the local defect. Figure 3c shows topographies of a Mn_{22} chain with an additional Mn atom, whose distance to the right chain end is varied. dI/dV spectroscopy on the left and right chain end as well as on the single atom reveals the coupling between both structures (Fig. 3d–f): as the single atom approaches the chain, its sub-gap spectral character is altered. The same holds for the right chain end, which directly interacts with the single atom because of their close proximity, i.e. the peak position of the end state slightly shifts. In contrast, the left chain end is not altered, proving that the end states are entirely local instead of collective properties of the chain. This is not expected for MMs or their precursors, where moving a magnetic atom close to one chain end merely laterally shifts the spatial location of the zero-energy end state on that side, or shifts the energy of the lowest-lying state simultaneously at both ends of the chain²⁷. Additional data provided in Supplementary Note 5 demonstrates that this is not the case, i.e. the spectral weight is not just laterally shifted. The observed energetical splitting of the two end states with respect to each other indicates that in the undisturbed chains, two states are localized, one at each end, which are degenerate due to the antiferromagnetic spin structure, in contrast to MMs or their precursors that form a single fermionic state with enhanced intensities at both ends.

Minimal model for antiferromagnetic YSR chains

To understand the nature of these trivial end states, we construct a minimal theoretical model for antiferromagnetic YSR chains. A single-particle model following refs. 3,4,6,22,23 successfully describes the sub-gap electronic bands in ferromagnetic YSR chains, especially when extended with local potential scattering^{27,32}. We extend these models by studying an antiferromagnetic chain on a superconducting substrate including Rashba SOC and arrive at the following minimal

next-nearest-neighbor model Hamiltonian (see Methods for details):

$$\mathcal{H} = -E_0 \sum_{i=1}^N c_i^\dagger c_i - t_1 \sum_{i=1}^{N-1} (c_i^\dagger c_{i+1} + \text{h.c.}) - t_2 \sum_{i=1}^{N-2} (c_i^\dagger c_{i+2} + \text{h.c.}) - \Delta_1 \sum_{i=1}^{N-1} (c_i^\dagger c_{i+1}^\dagger + \text{h.c.}) - \Delta_2 \sum_{i=1}^{N-2} (c_i^\dagger c_{i+2}^\dagger + \text{h.c.}). \quad (1)$$

Here, c_i^\dagger , c_i represent the creation and annihilation operators of YSR states at site i of a one-dimensional chain with N sites. The on-site energies $-E_0$ would correspond to the YSR state energies of the individual Mn impurity. The model includes nearest-neighbor (NN; index 1) and next-nearest-neighbor (NNN; index 2) hopping (t_1 , t_2) and superconducting pairing (Δ_1 , Δ_2) (Fig. 4a). The model connects to the Kitaev chain⁵¹ if only the NN terms are kept.

Notably, a perfectly collinear antiferromagnetic ordering is characterized by an ETRS (see Methods) consisting of physical time reversal inverting the spin directions and a translation by the distance between the chain atoms¹⁰. In the present Hamiltonian expressed in the basis of atomic YSR states, the ETRS implies that hopping terms are only allowed between atomic YSR states with the same spin, i.e. between NNNs in the present model (see Methods and Fig. 4a). In contrast, the effective superconducting pairing Δ_1 can easily be induced between adjacent atoms, since their spins are anti-aligned, and will be suppressed for NNNs (Δ_2), where the spins have a parallel alignment. For non-zero SOC these restrictions are lifted (see Methods), and the ratio of the coefficients induced by the SOC and present without the SOC may be estimated by the dimensionless parameter $\alpha_R/\hbar v_F$, where α_R is the Rashba parameter and v_F is the Fermi velocity. This parameter was estimated to be $k_h/k_{F,0} = 0.094$ for Mn/Nb(110) in ref. 27. We consequently pay particular attention to the case $t_1 \ll t_2$, and $\Delta_1 \gg \Delta_2$ of our minimal model and further assume $E_0 \approx 0.0$ meV, which is motivated by the experimental YSR state energies for $N=1,2,3$ (Fig. 1c).

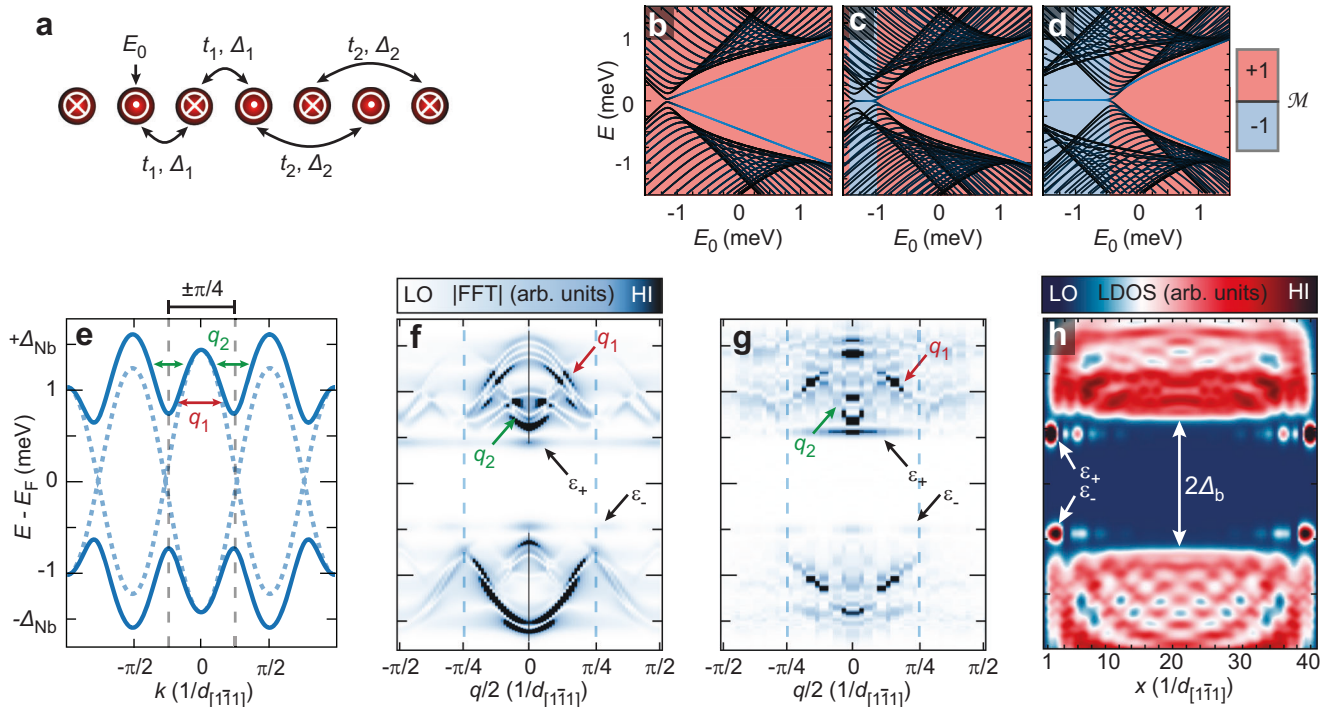


Fig. 4 | Minimal model for antiferromagnetic YSR chains and experimental QPI results. **a** Sketch of the parameters in an antiferromagnetically ordered chain considered in the minimal model of the YSR states. The symbols indicate up (\odot) and down (\otimes) oriented magnetic moments, respectively. t_1 (t_2) is the NN (NNN) hopping, Δ_1 (Δ_2) is the NN (NNN) pairing term and E_0 is the on-site energy (see Methods). **b** Eigenenergies of a finite-size chain with $N = 40$ for varying on-site energy E_0 and hopping parameters $t_1 = 0.0$ meV, $t_2 = 0.6$ meV. **c** Same as panel b, but with a small ETRS breaking term, $t_1 = 0.1$ meV, $t_2 = 0.6$ meV. **d** Same as **b** and **c**, but with an unrealistically large ETRS breaking term, $t_1 = 0.4$ meV, $t_2 = 0.6$ meV. $\Delta_1 = 0.5$ meV, $\Delta_2 = 0.0$ meV are chosen for all **b–d**. The Majorana number \mathcal{M} of the system is trivial (+1) in the red regions and non-trivial (–1) in the blue regions (see

Methods for details). The dark blue lines in panels b–d are end states of the system. **e** YSR band structure from the minimal model using the parameters $E_0 = 0.0$ meV, $t_1 = 0.1$ meV, $t_2 = 0.6$ meV, $\Delta_1 = 0.0$ meV (dashed lines) as well as $\Delta_1 = 0.5$ meV (solid lines), and $\Delta_2 = 0.0$ meV. The position of $k = \pm\pi/4$ is marked by dashed lines. **f** Absolute values of the line-wise FFT of a calculated LDOS line-profile similar to panel h using $N = 100$ sites. **g** Absolute values of the line-wise FFT of the experimental dI/dV line-profile in Fig. 1d. The supposed dispersive scattering vectors q_1 , q_2 and the edge state energies $\varepsilon_{+/-}$ are marked in **e–g**. **h** Calculated LDOS along a chain of $N = 40$ sites using the parameters from panels e and f. The energies of the finite-energy end states $\varepsilon_{+/-}$ and the chain's bulk minigap Δ_b are marked.

Experimentally, information about the sub-gap bands' dispersion can be extracted from one-dimensional quasiparticle interference (QPI) measurements^{27,32} (see Supplementary Note 6 and the extracted dispersion of the scattering vectors in Fig. 4g). We adjust the parameters of the minimal model such that the dispersions of the possible scattering vectors q_1 , q_2 in Fig. 4f extracted from the calculated dispersion in Fig. 4e reasonably fit the experimental dispersions of Fig. 4g. Using these parameters, we calculate the spatially resolved LDOS for various chain lengths N (Fig. 4h, Supplementary Fig. 6, and Methods) which, given the few free parameters, agree surprisingly well with the experimental data in Fig. 1c, d. In particular, the minimal model nicely reproduces the appearance of non-zero energy end states with an oscillatory decay towards the chain center at energies $\varepsilon_{+/-}$ in a large minigap Δ_b , the fast convergence of these end states towards $\varepsilon_{+/-}$ already for short chains (Supplementary Fig. 6), as well as the dispersive nature of the bulk states.

Having substantiated the minimal model by comparison to the experimental data, we investigate its parameter-dependent phases and the topological nature of the end states in the following. Figure 4b–d show the energy spectrum of a 40-site chain vs. the on-site energy E_0 for different values of the hopping terms t_1 and t_2 . It can be seen that the topologically non-trivial phase of the Kitaev chain is entirely quenched for $t_1 \rightarrow 0$ which corresponds to zero SOC (Fig. 4b). This is a consequence of the ETRS, which results in a Kramers degeneracy of all states, hence in a topologically trivial Majorana number. This finding agrees with previous studies, showing that topologically non-trivial phases cannot be found in antiferromagnetic YSR chains without

either strong SOC or additional supercurrents^{9,10} breaking the ETRS. However, it is found that the end states at finite energy are formed even in this topologically trivial regime for $t_2 > t_1$ whenever the gap is reopened by the superconducting term Δ_1 . Each of these end states is twofold degenerate for even-length chains and shows a small splitting for odd-length chains where the ETRS is broken. This prediction agrees well with the experimentally observed energy splittings in the regime $8 < N < 14$ for odd N in Fig. 1c. The degeneracy is restored for semi-infinite chains ($N \rightarrow \infty$). The fact that they merge with the continuum of states in Fig. 4b–d for large E_0 without a gap closure further proves their topologically trivial origin. For non-zero values of t_1 , corresponding to finite SOC, the non-zero-energy end states in some part of the topologically non-trivial phase are preserved (Fig. 4c). But now, also a topologically non-trivial phase with zero-energy MMs is recovered, which only takes up a large proportion of the phase space for unrealistically large values of SOC (Fig. 4d).

In conclusion, we have shown that the in-gap quasiparticle structure of dense, antiferromagnetic YSR chains can be qualitatively described by a minimal model. In contrast to ferromagnetic chains, the antiferromagnetic structure facilitates the formation of a large minigap in the YSR band even without SOC. This observation may be qualitatively explained by the fact that all YSR states in a ferromagnetic chain possess the same spin polarization, meaning that the s -wave superconducting pairing in the substrate may only open a gap in the spectrum for non-zero SOC. For the antiferromagnetic chain the localized YSR states at the sites have an alternating spin polarization, which enables pairing between these states without SOC and can lead

to a considerably larger minigap. This large size of the minigap naturally leads to a strong localization of potential end states, since their extension is inversely proportional to the minigap width^{27,52}. Therefore, antiferromagnetic chains appear to be more suitable for the realization of well-localized end states than their ferromagnetic counterparts. However, as visible from our simulations in Fig. 4b and as was shown in refs. 9 and 10, the formation of the topologically non-trivial phase now is a threshold effect: the SOC has to compete with the pairing potential, meaning that unrealistically large values of SOC have to be assumed in order to enable the formation of MMs. This is in contrast to the ferromagnetic chain, which is gapless in the absence of SOC and consequently an arbitrarily weak SOC may drive it into the topologically non-trivial regime. The most promising path towards combining the large minigap of antiferromagnetic chains with the easily achievable topologically non-trivial phases of ferromagnetic chains lies in the realization of YSR bands formed by non-collinear spin configurations^{24,53}.

Our minimal model furthermore reproduces the presence of intriguing finite-energy end states in the antiferromagnetic chains which are not topologically protected and whose energy can be tuned by local potentials. Notably, other experimental datasets on antiferromagnetic chains³⁴ show similar finite-energy end states, providing evidence that our findings are generally valid for other magnet-superconductor hybrids, too. A corresponding topologically trivial phase has been characterized by Pientka et al. as a two-channel p -wave superconducting wire where the interaction between two pairs of MMs lifts their energy to finite values and destroys their topological protection^{3,54}. However, we want to emphasize that this separation into two channels is not straightforward if SOC is present, and thus, this argument must not be taken at face value. Coincidentally, the trivial end states may appear at near-zero energy by local potentials where they could be misinterpreted as MMs. We have shown here that a local perturbation of the end states with defects is a distinct way to prove their topologically trivial or non-trivial nature. This methodology can be used on other sample systems to probe the stability of candidate topological edge modes against local disorder.

Methods

Experimental procedures

The experiments were performed in a home-built STM setup under ultra-high-vacuum at a base temperature of $T = 320$ mK⁵⁵. Nb(110) and Ta(110) single crystals were used as a substrate and cleaned by high-temperature flashes to $T > 2700$ K with an e-beam heater. In this way, atomically clean surfaces with only few residual oxygen impurities on the surface can be obtained for both materials, as shown previously^{39,56}. Subsequently, single Mn atoms were deposited onto the surface of the clean substrates held at low temperatures ($T < 7$ K), resulting in a statistical distribution of adatoms. We use superconducting Nb tips made from mechanically cut and sharpened high-purity Nb wire. The tips were flashed in situ to about 1500 K to remove residual contaminants. STM images were obtained by regulating the tunneling current I_{stab} to a constant value with a feedback loop while applying a constant bias voltage V_{stab} across the tunneling junction. For measurements of differential tunneling conductance (dI/dV) spectra, the tip was stabilized at bias voltage V_{stab} and current I_{stab} as individually noted in the figure captions. In a next step, the feedback loop was switched off and the bias voltage was swept from $-V_{\text{stab}}$ to $+V_{\text{stab}}$. The dI/dV signal was measured using standard lock-in techniques with a small modulation voltage V_{mod} (RMS) of frequency $f = 4.142$ kHz added to V_{stab} . dI/dV line-profiles and maps were acquired recording multiple dI/dV spectra along a one-dimensional line or a two-dimensional grid of lateral positions on the sample, respectively. Note that we chose stabilization parameters at which the contribution of Andreev reflections and direct Cooper pair tunneling can be neglected (see Supplementary Note 3). The use of superconducting Nb tips increases the effective energy resolution of the experiment beyond the

Fermi-Dirac limit⁵⁷. However, the differential tunneling conductance dI/dV measured with superconducting tips is proportional to the convolution of the sample's local density of states (LDOS) and the superconducting tip density of states (DOS). Consequently, STS data need to be numerically deconvoluted in order to resemble the sample's LDOS, as it is typically known for the interpretation of STS experiments. After careful deconvolution of the spectra, the superconducting gaps of the Nb and Ta surfaces are found to be $\Delta_{\text{Nb}} = 1.51$ meV and $\Delta_{\text{Ta}} = 0.64$ meV, respectively (see refs. 27,32 for Nb and Supplementary Fig. 3 for Ta). We show only deconvoluted data throughout the manuscript (see Supplementary Note 3 for details). Mn chains were constructed using lateral atom manipulation^{38,39} techniques at low tunneling resistances of $R \approx 30$ – 60 k Ω .

Minimal model for YSR bands in antiferromagnetic chains

Pientka et al. showed in ref. 3 that the low-energy electronic structure of a single-orbital chain of classical magnetic moments with a helical spin texture embedded in a three-dimensional superconducting host can be reduced to an effective Bogoliubov-de-Gennes Hamiltonian on a basis of projected YSR states. Subsequent models of the same type included Rashba-type SOC in ferromagnetic chains in refs. 2,4,6 and non-zero potential scattering and particle-hole asymmetric spectral weights in refs. 32,58. Here, we combine the SOC with non-zero potential scattering and a general spin structure, where the impurity atoms are assumed to be identical apart from the orientation of their classical spin. The effective Hamiltonian describing the YSR subgap band is given by

$$\mathcal{H} = \frac{1}{2} \sum_{ij} [\tilde{c}_i^\dagger \quad \tilde{c}_i] \begin{bmatrix} h_{ij} & \Delta_{ij} \\ -\Delta_{ij}^* & -h_{ij}^* \end{bmatrix} \begin{bmatrix} \tilde{c}_j \\ \tilde{c}_j^\dagger \end{bmatrix}, \quad (2)$$

with the matrix elements expressed as

$$h_{ij} = -E_0 \delta_{ij} + h_{ij}^{(0)} \langle \uparrow(i) | \uparrow(j) \rangle + h_{ij}^{(\alpha)} \langle \uparrow(i) | i\sigma^y | \uparrow(j) \rangle, \quad (3)$$

$$\Delta_{ij} = \Delta_{ij}^{(0)} \langle \uparrow(i) | \downarrow(j) \rangle + \Delta_{ij}^{(\alpha)} \langle \uparrow(i) | i\sigma^y | \downarrow(j) \rangle, \quad (4)$$

where E_0 is the single-impurity YSR energy. The real-valued coefficients $h_{ij}^{(0)}$, $h_{ij}^{(\alpha)}$, $\Delta_{ij}^{(0)}$ and $\Delta_{ij}^{(\alpha)}$ are material-specific constants, decaying with the distance $r = |\mathbf{r}_i - \mathbf{r}_j|$ as $\propto r^{-1} e^{ik_{\text{F}} r - r/\xi_0}$ for an isotropic electronic structure in three dimensions. Crucially, these terms do not depend on the magnetic structure of the chain but only on the electronic structure of the substrate and on the magnetic and non-magnetic scattering amplitudes of the impurities. Constants with superscript (0) remain finite at zero SOC, while the terms with superscript (α) vanish. Exemplary formulae for these coefficients are given in refs. 4,6. We refrain from giving their full form here since they are not used explicitly in this manuscript, where the coefficients are fit to the experimentally observed YSR band structure, remaining consistent with the above form. Following a similar analysis to ref. 4, the most important conclusion is that the (α) terms are linear in the dimensionless SOC parameter $\alpha_{\text{R}}/\hbar v_{\text{F}}$ in leading order, making them typically two orders of magnitude smaller than the (0) terms. Due to the oscillatory decay of the parameters with the distance, it might be possible but considerably difficult to design a system where the (α) and (0) terms have comparable magnitude; decreasing the Fermi velocity in flat bands may also provide a way for achieving this.

The magnetic structure only enters in the matrix elements of the vectors $|\uparrow(i)\rangle = (e^{-i\varphi_i/2} \cos\vartheta_i/2, e^{i\varphi_i/2} \sin\vartheta_i/2)$ and $|\downarrow(i)\rangle = (e^{-i\varphi_i/2} \sin\vartheta_i/2, -e^{i\varphi_i/2} \cos\vartheta_i/2)$, which are eigenvectors of the spin operator $\mathbf{S}_i \cdot \boldsymbol{\sigma}$ with $\mathbf{S}_i = (\sin\vartheta_i \cos\varphi_i, \sin\vartheta_i \sin\varphi_i, \cos\vartheta_i)$ describing the magnetization direction of the i th impurity. In Eqs. (3) and (4), the Pauli matrix σ^y enters due to the Rashba term when assuming that the chain is along the x direction; for a different chain direction or symmetry

4. Li, J. et al. Two-dimensional chiral topological superconductivity in Shiba lattices. *Nat. Commun.* **7**, 12297 (2016).
5. Schecter, M., Flensberg, K., Christensen, M. H., Andersen, B. M. & Paaske, J. Self-organized topological superconductivity in a Yu-Shiba-Rusinov chain. *Phys. Rev. B* **93**, 140503 (2016).
6. Brydon, P. M. R., Das Sarma, S., Hui, H.-Y. & Sau, J. D. Topological Yu-Shiba-Rusinov chain from spin-orbit coupling. *Phys. Rev. B* **91**, 064505 (2015).
7. Díaz, S. A., Klinovaja, J., Loss, D. & Hoffman, S. Majorana bound states induced by antiferromagnetic skyrmion textures. *Phys. Rev. B* **104**, 214501 (2021).
8. Lo Conte, R. et al. Coexistence of antiferromagnetism and superconductivity in Mn/Nb(110). *Phys. Rev. B* **105**, L100406 (2022).
9. Heimes, A., Kotetes, P. & Schön, G. Majorana fermions from Shiba states in an antiferromagnetic chain on top of a superconductor. *Phys. Rev. B* **90**, 060507 (2014).
10. Heimes, A., Mendler, D. & Kotetes, P. Interplay of topological phases in magnetic adatom-chains on top of a Rashba superconducting surface. *New J. Phys.* **17**, 023051 (2015).
11. Kobińska, A., Sedlmayr, N. & Ptok, A. Majorana bound states in a superconducting Rashba nanowire in the presence of antiferromagnetic order. *Phys. Rev. B* **103**, 125110 (2021).
12. Manna, S. et al. Interfacial superconductivity in a bi-collinear antiferromagnetically ordered FeTe monolayer on a topological insulator. *Nat. Commun.* **8**, 14074 (2017).
13. Aluru, R. et al. Atomic-scale coexistence of short-range magnetic order and superconductivity in $\text{Fe}_{1+y}\text{Se}_{0.1}\text{Te}_{0.9}$. *Phys. Rev. Mater.* **3**, 084805 (2019).
14. Fernandes, R. M. et al. Unconventional pairing in the iron arsenide superconductors. *Phys. Rev. B* **81**, 140501 (2010).
15. Heinrich, B. W., Pascual, J. I. & Franke, K. J. Single magnetic adsorbates on s-wave superconductors. *Prog. Surf. Sci.* **93**, 1–19 (2018).
16. Yazdani, A., Eigler, D. M., Lutz, C. P., Jones, B. A. & Crommie, M. F. Probing the local effects of magnetic impurities on superconductivity. *Science* **275**, 1767–1770 (1997).
17. Franke, K. J., Schulze, G. & Pascual, J. I. Competition of superconducting phenomena and Kondo screening at the nanoscale. *Science* **332**, 940–944 (2011).
18. Ruby, M., Heinrich, B. W., Peng, Y., Von Oppen, F. & Franke, K. J. Wave-function hybridization in Yu-Shiba-Rusinov dimers. *Phys. Rev. Lett.* **120**, 156803 (2018).
19. Beck, P. et al. Spin-orbit coupling induced splitting of Yu-Shiba-Rusinov states in antiferromagnetic dimers. *Nat. Commun.* **12**, 2040 (2021).
20. Choi, D.-J. et al. Influence of magnetic ordering between Cr adatoms on the Yu-Shiba-Rusinov states of the $\beta\text{-Bi}_2\text{Pd}$ superconductor. *Phys. Rev. Lett.* **120**, 167001 (2018).
21. Kim, Y., Zhang, J., Rossi, E. & Lutchyn, R. M. Impurity-induced bound states in superconductors with spin-orbit coupling. *Phys. Rev. Lett.* **114**, 236804 (2015).
22. Röntynen, J. & Ojanen, T. Topological superconductivity and high Chern numbers in 2D ferromagnetic Shiba lattices. *Phys. Rev. Lett.* **114**, 236803 (2015).
23. Röntynen, J. & Ojanen, T. Chern mosaic: Topology of chiral superconductivity on ferromagnetic adatom lattices. *Phys. Rev. B* **93**, 094521 (2016).
24. Kim, H. et al. Toward tailoring Majorana bound states in artificially constructed magnetic atom chains on elemental superconductors. *Sci. Adv.* **4**, eaar5251 (2018).
25. Nadj-Perge, S. et al. Observation of Majorana fermions in ferromagnetic atomic chains on a superconductor. *Science* **346**, 602–607 (2014).
26. Kezilebieke, S. et al. Topological superconductivity in a van der Waals heterostructure. *Nature* **588**, 424–428 (2020).
27. Schneider, L. et al. Precursors of Majorana modes and their length-dependent energy oscillations probed at both ends of atomic Shiba chains. *Nat. Nanotechnol.* **17**, 384–389 (2022).
28. Palacio-Morales, A. et al. Atomic-scale interface engineering of Majorana edge modes in a 2D magnet-superconductor hybrid system. *Sci. Adv.* **5**, eaav6600 (2019).
29. Beck, P., Schneider, L., Wiesendanger, R. & Wiebe, J. Effect of substrate spin-orbit coupling on the topological gap size of Shiba chains. *arXiv:2205.10062*. (2022).
30. Ruby, M. et al. End states and subgap structure in proximity-coupled chains of magnetic adatoms. *Phys. Rev. Lett.* **115**, 197204 (2015).
31. Ruby, M., Heinrich, B. W., Peng, Y., von Oppen, F. & Franke, K. J. Exploring a proximity-coupled Co chain on Pb(110) as a possible Majorana platform. *Nano Lett.* **17**, 4473–4477 (2017).
32. Schneider, L. et al. Topological Shiba bands in artificial spin chains on superconductors. *Nat. Phys.* **17**, 943–948 (2021).
33. Liebhaber, E. et al. Quantum spins and hybridization in artificially-constructed chains of magnetic adatoms on a superconductor. *Nat. Commun.* **13**, 2160 (2022).
34. Küster, F. et al. Non-Majorana modes in diluted spin chains proximitized to a superconductor. *Proc. Natl. Acad. Sci.* **119**, 2112.05708 (2022).
35. Mier, C. et al. Atomic manipulation of in-gap states in the $\beta\text{-Bi}_2\text{Pd}$ superconductor. *Phys. Rev. B* **104**, 045406 (2021).
36. Schneider, L. et al. Controlling in-gap end states by linking non-magnetic atoms and artificially-constructed spin chains on superconductors. *Nat. Commun.* **11**, 4707 (2020).
37. Eigler, D. M. & Schweizer, E. K. Positioning single atoms with a scanning tunnelling microscope. *Nature* **344**, 524–526 (1990).
38. Schneider, L., Beck, P., Wiebe, J. & Wiesendanger, R. Atomic-scale spin-polarization maps using functionalized superconducting probes. *Sci. Adv.* **7**, eabd7302 (2021).
39. Beck, P., Schneider, L., Wiesendanger, R. & Wiebe, J. Systematic study of Mn atoms, artificial dimers, and chains on superconducting Ta(110). *Phys. Rev. B* **107**, 024426 (2023).
40. Nyári, B. et al. Relativistic first-principles theory of Yu-Shiba-Rusinov states applied to Mn adatoms and Mn dimers on Nb(110). *Phys. Rev. B* **104**, 235426 (2021).
41. Crawford, D. et al. Majorana modes with side features in magnet-superconductor hybrid systems. *npj Quantum Mater.* **7**, 117 (2022).
42. Lászlóffy, A., Palotás, K., Rózsa, L. & Szunyogh, L. Electronic and magnetic properties of building blocks of Mn and Fe atomic chains on Nb(110). *Nanomaterials* **11**, 1933 (2021).
43. Crawford, D. et al. Increased localization of Majorana modes in antiferromagnetic chains on superconductors. *Phys. Rev. B* **107**, 075410 (2023).
44. Feldman, B. E. et al. High-resolution studies of the Majorana atomic chain platform. *Nat. Phys.* **13**, 286–291 (2017).
45. Schneider, L. et al. Magnetism and in-gap states of 3d transition metal atoms on superconducting Re. *npj Quantum Mater.* **4**, 42 (2019).
46. Ruby, M., Peng, Y., von Oppen, F., Heinrich, B. W. & Franke, K. J. Orbital picture of Yu-Shiba-Rusinov multiplets. *Phys. Rev. Lett.* **117**, 186801 (2016).
47. Odobesko, A. et al. Observation of tunable single-atom Yu-Shiba-Rusinov states. *Phys. Rev. B* **102**, 174504 (2020).
48. Liebhaber, E. et al. Yu-Shiba-Rusinov states in the charge-density modulated superconductor NbSe₂. *Nano Lett.* **20**, 339–344 (2020).
49. Khajetoorian, A. A. et al. Tuning emergent magnetism in a Hund's impurity. *Nat. Nanotechnol.* **10**, 958–964 (2015).
50. Mier, C., Choi, D.-J. & Lorente, N. Moiré dispersion of edge states in spin chains on superconductors. *Phys. Rev. Res.* **4**, L032010 (2022).

51. Kitaev, A. Y. Unpaired Majorana fermions in quantum wires. *Physics-Uspekhi* **44**, 131–136 (2001).
52. Peng, Y., Pientka, F., Glazman, L. I. & von Oppen, F. Strong localization of Majorana end states in chains of magnetic adatoms. *Phys. Rev. Lett.* **114**, 106801 (2015).
53. Klinovaja, J., Stano, P., Yazdani, A. & Loss, D. Topological superconductivity and Majorana fermions in RKKY systems. *Phys. Rev. Lett.* **111**, 186805 (2013).
54. Pientka, F., Glazman, L. I. & von Oppen, F. Unconventional topological phase transitions in helical Shiba chains. *Phys. Rev. B* **89**, 180505 (2014).
55. Wiebe, J. et al. A 300 mK ultra-high vacuum scanning tunneling microscope for spin-resolved spectroscopy at high energy resolution. *Rev. Sci. Instrum.* **75**, 4871–4879 (2004).
56. Odobesko, A. B. et al. Preparation and electronic properties of clean superconducting Nb(110) surfaces. *Phys. Rev. B* **99**, 115437 (2019).
57. Pan, S. H., Hudson, E. W. & Davis, J. C. Vacuum tunneling of superconducting quasiparticles from atomically sharp scanning tunneling microscope tips. *Appl. Phys. Lett.* **73**, 2992–2994 (1998).
58. von Oppen, F., Peng, Y. & Pientka, F. in *Topological Aspects of Condensed Matter Physics* 387–450 (Oxford Univ. Press, 2014).

Acknowledgements

We thank Eric Mascot, Roberto Lo Conte and Falko Pientka for helpful discussions. L.S., T.P., J.W., and R.W. gratefully acknowledge funding by the Cluster of Excellence ‘Advanced Imaging of Matter’ (EXC 2056 - project ID 390715994) of the Deutsche Forschungsgemeinschaft (DFG). L.R. gratefully acknowledges financial support from the National Research, Development and Innovation Office of Hungary via Project Nos. K131938 and FK142601, from the Ministry of Culture and Innovation and the National Research, Development and Innovation Office within the Quantum Information National Laboratory of Hungary (Grant No. 2022-2.1.1-NL-2022-00004) and from the Young Scholar Fund at the University of Konstanz. P.B., J.W. and R.W. acknowledge support by the DFG (SFB 925—project 170620586). R.W. acknowledges funding by the European Union via the ERC Advanced Grant ADMIRE (project No. 786020). T.P. acknowledges support by the DFG (project no. 420120155).

Author contributions

L.S., P.B., R.W. and J.W. conceived the experiments. L.S. and P.B. performed the measurements and analyzed the experimental data. L.S. performed the numerical simulations in close exchange with T.P. and

L.R. L.S. prepared the figures and wrote the manuscript. All authors contributed to the discussions and to correcting the manuscript.

Funding

Open Access funding enabled and organized by Projekt DEAL.

Competing interests

The authors declare no competing interests.

Additional information

Supplementary information The online version contains supplementary material available at <https://doi.org/10.1038/s41467-023-38369-w>.

Correspondence and requests for materials should be addressed to Jens Wiebe.

Peer review information *Nature Communications* thanks Yonglong Xie, and the other, anonymous, reviewer(s) for their contribution to the peer review of this work. A peer review file is available.

Reprints and permissions information is available at <http://www.nature.com/reprints>

Publisher’s note Springer Nature remains neutral with regard to jurisdictional claims in published maps and institutional affiliations.

Open Access This article is licensed under a Creative Commons Attribution 4.0 International License, which permits use, sharing, adaptation, distribution and reproduction in any medium or format, as long as you give appropriate credit to the original author(s) and the source, provide a link to the Creative Commons license, and indicate if changes were made. The images or other third party material in this article are included in the article’s Creative Commons license, unless indicated otherwise in a credit line to the material. If material is not included in the article’s Creative Commons license and your intended use is not permitted by statutory regulation or exceeds the permitted use, you will need to obtain permission directly from the copyright holder. To view a copy of this license, visit <http://creativecommons.org/licenses/by/4.0/>.

© The Author(s) 2023